



## Supplementary Material for

### **Dating the Moon-forming impact event with asteroidal meteorites**

W. F. Bottke,\* D. Vokrouhlický, S. Marchi, T. Swindle, E. R. D. Scott, J. R. Weirich,  
H. Levison<sup>1</sup>

\*Corresponding author. E-mail: [bottke@boulder.swri.edu](mailto:bottke@boulder.swri.edu)

Published 17 April 2015, *Science* **348**, 321 (2015)

DOI: 10.1126/science.aaa0602

**This PDF file includes:**

Materials and Methods

Figs. S1 to S11

Table S1

Full Reference List

## Materials and Methods

### Sec. 1. Calculating Shock Degassing Age Profiles for GI Ejecta Hitting (4) Vesta

In this section, we discuss our methodology for calculating shock degassing ages. Additional details can be found in (12).

**Dynamics of giant impact ejecta.** The dynamical evolution of our GI ejecta test bodies was discussed in Fig. 1, though additional details are found Fig. S1. The interested reader is also encouraged to see (14) for a thorough discussion of these issues; we consider our work complementary to their work.

As discussed in Fig. 1, we started with 5 groups of 6,000 test bodies, with each group given an initial ejection velocity “at infinity” of 1, 3, 5, 7, or 9 km/s. When calculating collision probabilities and impact velocities between these test bodies and Vesta, or among the bodies themselves, we used all the data in each of the five sets. Our results, in the form of probability distributions, were then combined by weighting the contributions according to the initial velocity distribution set by GI hydrocode simulations; 14%, 27%, 26%, 18%, and 15% of the objects were assumed to be ejected at 1, 3, 5, 7, 9 km/s, respectively (14). Our method allows us to readily use different initial ejection velocity distributions if they become available.

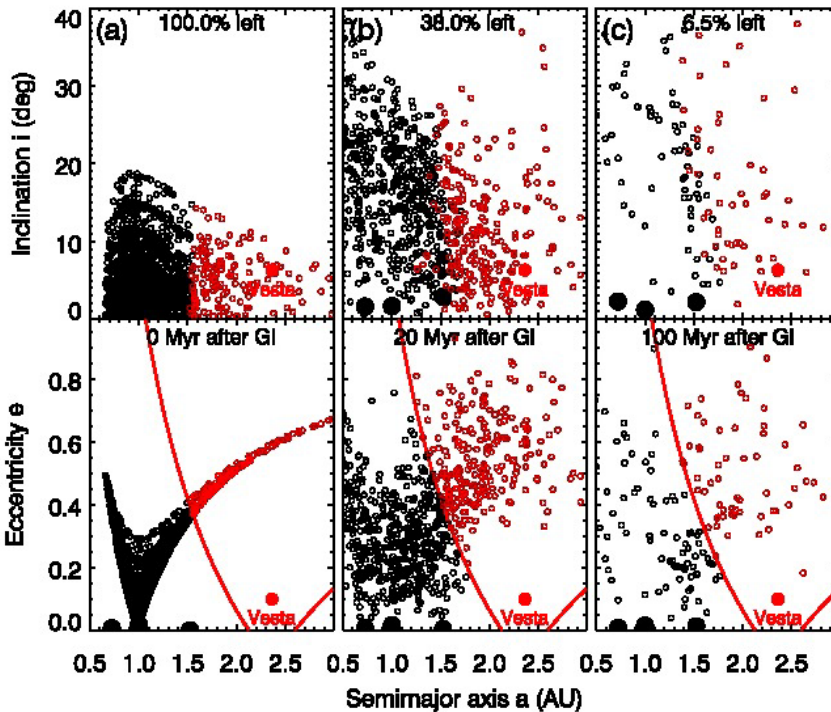


**Fig. S1.** The dynamical evolution of GI ejecta from Fig. 1. The initial conditions of the planets and test bodies are discussed in the main text and Fig. 1. The black and red test bodies show the same set of test bodies as Fig. 1 for evolution times of (a) 0, (b) 20, and (c) 100 Myr after the GI. Red test bodies have reached orbits that allow them to potentially hit Vesta, our representative main belt asteroid. The values provided at the top of the three top panels provide the fraction of our sampled test bodies left in the simulation, with the evolution time provided at the top of the bottom three panels.

By combining our results in this manner, we found most test bodies were eliminated by striking the Earth (30%), Venus (37%), or Mars (1%). Many of the longest-lasting ones were found to achieve high inclinations; this lowers their collision probabilities with the planets. The rest of the test bodies were lost when they hit the Sun or were ejected out of the inner solar system via a Jupiter encounter.

### Collision probabilities and impact velocities between giant impact ejecta and Vesta.

A critical issue in testing our hypothesis was to determine whether collisions between kilometer-sized GI ejecta fragments and main belt asteroids are plausible. As a first step to determining this, we used our dynamical evolution runs (Figs. 1, S1) and the formalism of (23) to calculate the intrinsic collision probabilities ( $P_i$ ) and impact velocity distributions between GI test bodies and a representative main belt asteroid, Vesta. We assumed the primordial Vesta had the same orbital parameters as its current proper elements: semimajor axis, eccentricity, and sine of the inclination of 2.3615 AU, 0.0994, and 0.1106, respectively. Fig. S2 shows representative values from our results, with the calculations shown at every 0.01 Myr timestep.

The  $P_i$  values, in units of  $10^{-18} \text{ km}^{-2} \text{ yr}^{-1}$ , were found to increase after a few Myr of evolution time as more GI bodies were scattered onto Vesta-crossing orbits by planetary encounters and resonances. Mean impact velocities, in units of km/s, also increase as the surviving test bodies were driven onto more eccentric and inclined orbits by planetary perturbations and dynamical resonances. After  $\sim 10$  Myr, the majority of impacts between GI ejecta and asteroids occur at mean impact velocities of  $\sim 10$  km/s. These events are likely to produce high impact temperatures and an abundance of  $^{40}\text{Ar}$ - $^{39}\text{Ar}$  shock degassing ages within their craters' breccia lenses and/or ejecta blankets (12) (see below).

Using these values with several approximations that are justified below, one can compute the approximate number of collisions on Vesta caused by GI ejecta immediately after the GI event:

- Vesta has a diameter of 530 km.

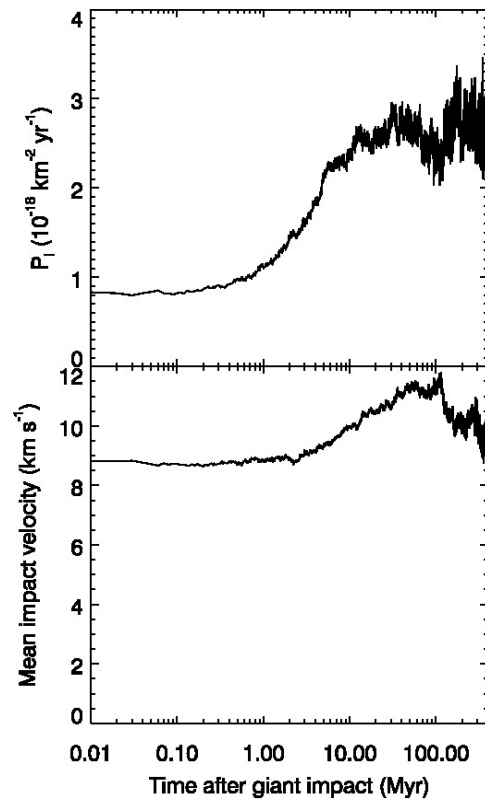


**Figure S2.** The intrinsic collision probability ( $P_i$ ) and mean impact velocities of GI ejecta striking Vesta.  $P_i$  values were multiplied at each timestep by the number of GI test bodies that cross Vesta's orbit over the number left in the population (e.g., Fig. S1).

- The GI event produced on the order of  $\sim 10^{10}$   $D > 1$  km diameter projectiles (Fig. S8).
- Collisional and dynamical evolution among the  $D > 1$  km GI population causes it to decrease to  $5 \times 10^7$  between 0-1 Myr after the GI (Fig. S8).

The number of impacts on Vesta over the first 1 Myr from  $D > 1$  km projectiles should be on the order of 10. This value is comparable to the number of  $D > 1$  km projectiles hitting Vesta over a  $\sim 100$  Myr interval in the present-day main belt (i.e., derived using the methods and results of 23, 30).

**Impact heating produced by high velocity projectiles.** The nature of impact heating on asteroids was explored in (12) and references therein. They found that the peak temperatures and volumes of target material heated above a given threshold (e.g., the closure temperature for Ar loss, causing age reset) were strongly dependent on impact velocity  $V$ . The key point for this work is that the estimated volume of shocked material raised above the reference temperature of 1000 K was found to be minimal for impacts at the average main belt velocity of  $\sim 5$  km/s, while it increased by many orders of magnitude for  $V > 10$  km/s (Fig. S3). Moreover,  $V > 10$  km/s impacts are needed to produce significant heating in the region between the excavation and transient crater depths or at greater depth. In other words, if all other parameters remain the same, most of the  $^{40}\text{Ar}$ - $^{39}\text{Ar}$  shock degassing ages in Fig. 2a were produced by high-velocity impactors.

As the color contour plots of impact velocity demonstrate in Fig. 1, high-velocity impacts on Vesta are rare in the current main belt. This probably explains the lack of impact melt found among stony meteorites, and why little impact melt has been identified within Vestan craters (9-11). To reach  $V > 10$  km/s, projectiles often need sizable inclinations, which are rare in the current main belt, and/or eccentricities larger than 0.5, which takes them out of the main belt entirely and onto planet-crossing orbits. Such eccentric impactors, however, only have dynamical lifetimes of a few Myr to a few tens of Myr (e.g., 13, 17, 22). This leaves them little time to strike small targets like main belt asteroids.

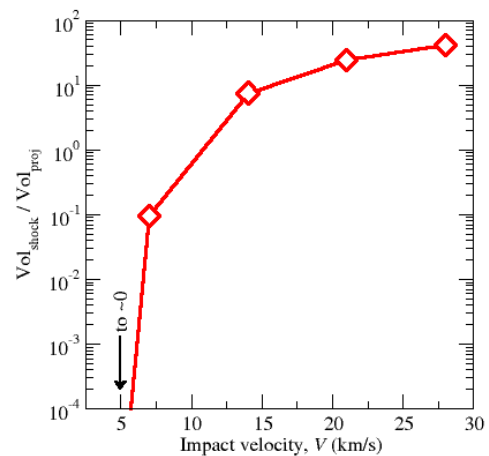


**Figure S3.** Hydrocode- based computations of impact heating for various collision velocities (6). The y-axis is the volume of shocked material ( $Vol_{shock}$ ) reaching or exceeding 1000 K over impactor volume ( $Vol_{proj}$ ).

**Asteroid impact heating profile.** To calculate the shock degassing age profile for GI ejecta hitting Vesta, we combined the components above with:

- Dynamical decay curves for the GI population. Using the test body dynamical evolution results for GI ejecta (Figs. 1, S1), we calculated how the population decreases over time by bodies impacting the Sun, the planets, or how they are thrown out of the inner solar system by a close encounter with Jupiter. Our results are shown in Fig. S4. After 250 Myr, less than 1% of the population remains in the inner solar system.
- Collisional evolution for many possible initial size frequency distributions (SFDs). An example of how collisional evolution might work for GI ejecta is shown in Fig. S8.

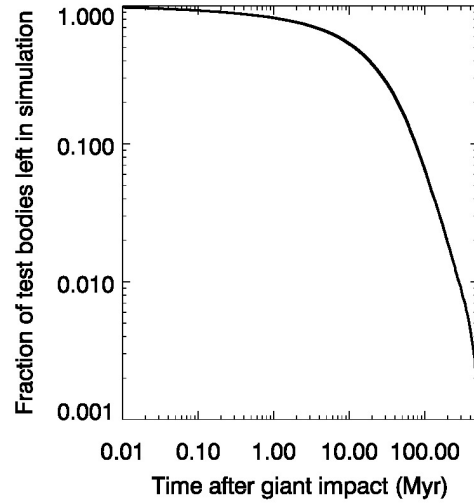


**Figure S4.** The dynamical decay of test bodies from our GI ejecta simulations.

After numerous tests using different starting SFDs, and as a compromise across these possibilities, we included the effects of collisions by dividing our values from Fig. S2 by a weighting factor distribution. Representative factor values at 2, 8, 20, and 100 Myr were 4, 2.3, 1.7, and 1, respectively.

Putting everything together yielded the profile shown in Fig. S5. The ~8 Myr delay needed to reach the peak is a byproduct of orbital evolution among the GI test bodies; it takes many of them this amount of time to reach a main belt-crossing orbit and to achieve high enough impact velocities with asteroids to produce  $^{40}\text{Ar}$ - $^{39}\text{Ar}$  ages (see Figs. 1, S1, S2).

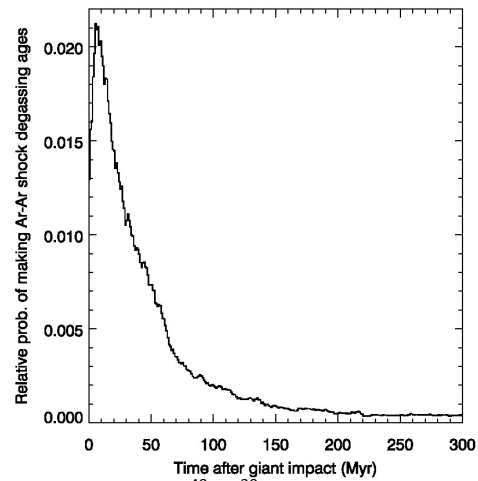


**Figure S5.** The  $^{40}\text{Ar}$ - $^{39}\text{Ar}$  shock degassing age profile produced when GI ejecta hits our representative asteroid Vesta.

## **Sec. 2. The initial size distribution and collisional evolution of giant impact ejecta**

Small bodies populations in the terrestrial planet region that are massive, numerous, and dynamically excited undergo rapid collisional evolution (e.g., 7, 30-31). Accordingly, our choice of a starting GI ejecta SFD and how it collisionally and dynamical evolves will play a critical role in our results. Here we discuss these issues in more detail.

**Choosing a giant impact scenario.** Many GI simulations show that several percent of an Earth mass is ejected completely out of the Earth-Moon system (3-5). Its physical state, however, is a mixture of solid material and vapor, with the ratio dependent on the GI event in question.

In the canonical GI that uses a Mars-sized impactor to make the Moon, most ejecta is in the form of solid debris (3). In two new higher energy GI simulations, vapor production is much larger, though a substantial fraction of solids can still be produced (4-5).

The appropriate GI simulation to use here is unknown, with all known GI events having problematic issues (32-33). For example, the canonical GI can readily match the angular momentum constraints of the Earth-Moon system, but most of the Moon comes from the projectile (3). This is surprising when one considers that the Earth and Moon have nearly identical oxygen isotopes, as well as close similarities in many other isotopes (e.g., 34). It is possible that the proto-Earth and projectile had similar isotopic compositions, as discussed in (34), but at present this constraint presents a challenge for planet formation models.

Additional flavors of GI events have been proposed to deal with Earth-Moon isotopic constraints. For example, in one scenario, a proto-Earth spinning once per two hours gets hit by a sub-Mars-mass body, with the impact trajectory appropriate to create a protolunar disk (and Moon) from material primarily derived from Earth's mantle (4). In another, two half-Earths collide with one another, with the subsequent Earth and protolunar disk made from a thorough mixture of the two compositions (5). Both models initially violate angular momentum constraints of the Earth-Moon system, such that they need the Moon to become trapped in the evection resonance to drain away excess angular momentum from the Earth-Moon system (4).

A potential problem with these high energy GI models is that it is yet unclear whether the formulation of the evection resonance discussed in (4) will work in similar ways if different protolunar disk and tidal evolution models are invoked. Careful modeling of the Moon's formation and evolution from a protolunar disk as well as the evection resonance trapping process itself is on-going (e.g., 33, 35-36).

A second potential problem is that the high energy GIs discussed above are thought to be low probability events in terms of planet formation models (32-33). For example, in the

first scenario above (4), getting the proto-Earth to reach a spin period of two hours requires a near-GI event, but one that cannot create even a small moon. If a moon is formed, it will readily remove rotational angular momentum from the proto-Earth via tidal interactions, thereby preventing the initial rotation conditions for the Earth that would produce our Moon in the proposed GI. Accordingly, the near-GI must spin the proto-Earth right up to the brink of substantial mass shedding without going over the threshold; this is challenging from an input parameter standpoint. In the second scenario above (5), the probability that two half-Earths hit and mix in the planet formation process is only on the order of 10%.

Finally, a third potential problem for the high energy GIs is that they may have experienced more mixing in the near-GI or GI itself than the geochemical constraints can tolerate (e.g., 37-38). Interestingly, the canonical impact does not experience substantial mixing, and therefore could pass tests that call for a heterogeneous Earth after the GI.

The bottom line is that while our Moon could certainly be a statistical anomaly, with several low probability events taking place, it is also possible that the potential issues above are an indication that something crucial is missing in our understanding of planet formation, lunar/terrestrial constraints, and/or the GI. Accordingly, we believe some latitude exists at this time in choosing GI outcomes, and we favor those that produce an abundance of solid ejecta. In fact, this work may represent an intriguing constraint on the nature of the GI that did take place.

**GI ejecta striking the Moon.** To glean insights into the kinds of GI ejecta SFDs that are plausible, we take advantage of the fact that GI ejecta came back to strike the Moon almost immediately after the Moon-forming event took place (e.g., 14). Here we quantify this scenario in order to use the Moon's ancient but well preserved basin record to constrain the nature of the initial GI ejecta SFD.

The GI ejecta runs used here are discussed in Figs. 1 and S1. As shown in Fig. S4, 50%, 90%, and 99% of the population was dynamically eliminated after 12, 76, and 248 Myr. Unlike typical asteroid evolution simulations, however, the majority are removed by hitting Venus or Earth (Sec. 1). Over 30% of the test bodies returned to hit the Earth, with 50%, 90% and 99% of them hitting within 3, 50, and 220 Myr.

The fraction of GI test bodies that hit the Moon was estimated using the formalism of (39). Their method requires us to input two sets of variables. The first set, the relative velocity of the GI impactors when they enter Earth's Hill sphere, was provided by the results of our dynamical runs (Figs. 1 and S1). The second set was the Moon's distance from Earth at a given time after the GI. This was computed using the Earth-Moon tidal evolution model results of (40), though we caution that the Moon's recession rate depends on unknown early dissipation within the primordial Earth. Because there are

reasons to think Earth's dissipation was far lower than at present, and that the Moon had a slow outward evolution, we tested two evolutionary pathways for the Moon: a more conservative one where it went from  $\sim 10$  to  $\sim 30$  Earth radii over 400 Myr and a slower one where it traveled from 6 to  $\sim 20$  Earth radii over 400 Myr (41).

Both lunar evolution pathways were found to yield similar results, with the Moon accreting 0.8-0.9% of our GI test bodies. These values will be used below.

**Initial size distribution for giant impact ejecta.** To select a reasonable GI ejecta size frequency distribution (SFD), we would ideally select results directly from numerical hydrocode experiments of the GI that reproduce Earth-Moon system constraints. Unfortunately, the smallest particles in these simulations are often on the order of hundreds of km in diameter (3-5, 42). For this reason, we turn to the lunar impact record itself to winnow our possible initial SFD.

Working from the largest bodies to the smallest, we start with the results of (12), who argue that the largest fragments in their GI simulations were on the order of  $D \sim 600$  km. We adopt this size as a reasonable top end for our GI ejecta SFD.

Next, we consider the constraint provided by South-Pole Aitken (SPA) basin, the largest undisputed lunar impact structure with a diameter of 2,400 by 2,100 km. Hydrocode impact simulations show it was made from a  $D \sim 170$  km impactor striking the Moon at  $\sim 10$  km/s (43). Given that GI test body accretion with the Moon is 0.8-0.9%, and  $D > 170$  km bodies are relatively difficult to collisionally disrupt (Fig. S8), we predict the initial GI ejecta SFD had -- at most -- a few hundred of these bodies (i.e., a single SPA basin divided by the lunar impact probability of  $\sim 1\%$ ; if more  $D > 170$  km bodies were present, the Moon would have more SPA-like basins). For reference, this is comparable to the number of  $D > 170$  km bodies in the present-day main belt (30).

For  $D < 170$  km, we note that the oldest lunar surfaces (i.e., Pre-Nectarian surfaces) do not have many Imbrium- or Orientale-sized basins (900-1,200 km in diameter) (16, 44-45). This observation is surprising given the work of (45), who found that projectiles striking the high heat flux nearside regions of the Moon (i.e., the Procellarum KREEP terrain) make basins twice as large as those made on the cooler and thicker farside of the Moon. Presumably, just after the Moon formed, large impactors would have had little difficulty making enormous basins by hitting a thin warm crust with a high heat flux. The absence of such mega-basins suggests that there was a relative paucity of middle-sized projectiles in GI ejecta. Accordingly, we assume the power-law slope of the GI ejecta SFD was very shallow between  $D \sim 170$  km and a few tens of km (though it could also be that no GI ejecta fragments ever existed in this size range).

The Moon has  $\sim 25$  pre-Nectarian basins ( $D > 300$  km craters) (16; see also 44-45). If we assume they were made by  $D > 20$  km projectiles (e.g., 46), it would imply that the

number of initial GI fragments with  $D > 20$  were limited to –at best -- a few thousand at best (i.e., the order of 25 basin-producing projectiles divided by the lunar impact probability of  $\sim 1\%$ ). As above, this number is comparable to that in the current main belt population (30). We will show below that relatively few  $D > 20$  km bodies are expected to disrupt via collisional evolution.

Taking these values together as upper limits, we find the GI population for  $D > 20$  km bodies was comparable to or, more likely, much less than the mass of the current main asteroid belt ( $\sim 0.05\%$  that of the Earth) (Fig. S8). Accordingly, if GI ejecta once contained several percent of an Earth mass, a considerable fraction would have been in the form of  $D < 20$  km fragments. To this end, for  $D < 20$  km bodies, we tested SFDs with steep cumulative power law slopes between  $-4.5$  and  $-6$  (Fig. S8).

**Supporting evidence for steep fragment size frequency distribution for giant impact ejecta.** While the inferred steep SFD presented here appears to be somewhat radical, it actually fits well within a pattern of behavior derived from impacts on large stony bodies.

As an example, consider the results from (6, 47), who simulated impacts into 100-km diameter asteroids using a 3-D smooth-particle hydrodynamics (SPH) code combined with an  $N$ -body code. They found that impacts too small to produce catastrophic disruption events, defined as a collision that sends 50% of the ejecta away at escape velocity, will produce steep ejecta SFDs. The steepest SFDs made in their runs were created by cratering events, specifically when the parent body was left largely intact and when  $f_{\text{SFD}}$ , the ratio of the diameter of the remnant parent body to the largest fragment, was large (see *ref. 9* for a complementary discussion of this issue). Given their numerical resolution limitations, the steepest SFD derived in their simulations was for  $f_{\text{SFD}} \sim 20$ . They also found ejecta SFDs with  $f_{\text{SFD}} \sim 10$ -20 that matched those of several known asteroid families (e.g., the Eunomia family).

Interestingly, families associated with very large asteroids can have  $f_{\text{SFD}} > 20$ . Perhaps the best example in nature comes from the Vesta asteroid family, most which was produced in the same collision that created the  $\sim 500$  km diameter Rheasilvia basin (e.g., 18). We find Vesta’s family fragment SFD not only has  $f_{\text{SFD}} \sim 70$ , but it has remarkably steep slopes, with cumulative power law exponents of  $-3.7$  and  $-8$  for diameter  $D > 3$  km and  $D > 5$  km bodies, respectively (Fig. S6). These values are similar to those deduced for our GI ejecta SFD.

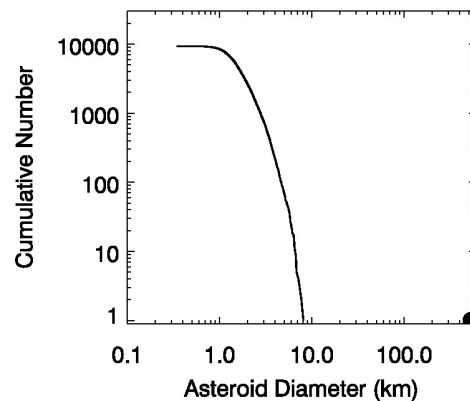


**Figure S6.** Size-frequency distribution for asteroid Vesta and its inferred family (15).

Vesta is large enough that it is almost impossible to catastrophically disrupt unless the projectile size is nearly the same size or larger than Vesta (30, 48-49). This “gravitational prevention of disruption” trend is even more pronounced for protoplanets and planetary embryos, and it suggests that even the largest GI impact events are technically cratering events in terms of the nature of the ejecta SFDs produced.

Accordingly, if we assume GI ejecta did not make SPA basin, and the steep branch of our initial SFD in Fig. S8 was a power law that extended down to a single large fragment, its size would be  $D \sim 70\text{-}100$  km (Fig. S8). This would make the value of  $f_{\text{SFD}}$  comparable to the diameter of the Earth (12,700 km) divided by 70-100 km, or  $\sim 130\text{-}180$ . This value is only 1.8-2.6 times that derived for the Vesta family. When combined with our work above, we argue that the GI ejecta SFD was steep at small sizes. These SFDs also imply that considerable mass was in the form of  $D > 0.1$  km bodies rather than being dominated by boulders and dust.

**Collisional evolution of giant impact ejecta.** Our next task is to determine how the fragments in our GI ejecta SFD undergo collisional evolution with themselves. This meant calculating the collision probabilities and impact velocities taking place between representative GI ejecta fragments hitting themselves. Using the dynamical evolution runs described in Fig. 1, we calculated the  $P_i$  and mean impact velocity ( $V$ ) distributions between the semimajor axes, eccentricities, and inclinations of our GI test bodies every 0.01 Myr, once again using the formalism described in (23). Our results are shown in Fig. S7.

The  $P_i$  values show a steep decline within the first few Myr, while  $V$  undergoes a sharp increase. This takes place for two reasons: the test bodies most likely to strike one another tend to be those on very Earth- or Venus-like orbits, which are quickly removed from the system, and scattering events among objects likely to encounter the terrestrial planets, along with dynamical resonances, quickly excite the surviving population to higher eccentricities and inclinations (Figs. 1 and S1).

Overall, the  $(P_i, V)$  values were found to be  $(190 \times 10^{-18} \text{ km}^{-2} \text{ yr}^{-1}, 7 \text{ km/s})$  after ejection, though test body excitation via planetary encounters and

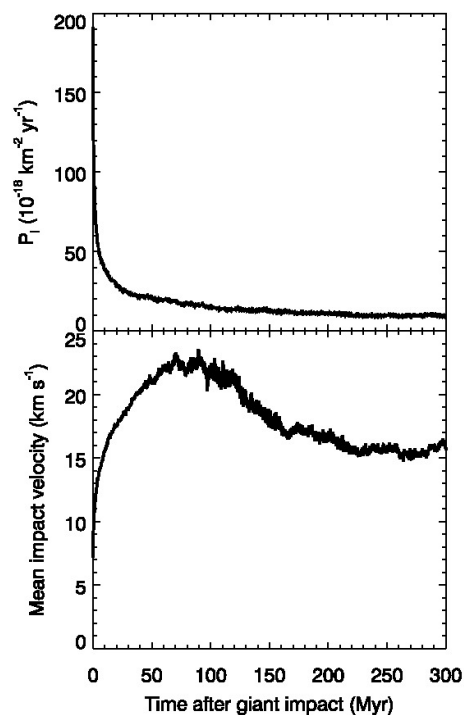


**Figure S7.** The intrinsic collision probabilities and impact velocities for test bodies ejected in the GI event striking one another.

resonances, combined with the removal of low eccentricity and inclination test bodies via planetary collisions, modified these values to  $(25 \times 10^{-18} \text{ km}^{-2} \text{ yr}^{-1}, 19 \text{ km/s})$  at 30 Myr and  $(15 \times 10^{-18} \text{ km}^{-2} \text{ yr}^{-1}, 22 \text{ km/s})$  at 100 Myr, respectively.

All of these components (i.e., the collision probability and impact velocity distributions from Fig. S7, the population decay rate from Fig. S4, and a variety of initial SFDs) were input into the collisional and dynamical depletion evolution model *Boulder* (19). This allowed us to track how the GI population changed in a physically realistic manner over hundreds of Myr. The disruption scaling relationships for GI ejecta striking one another were assumed to follow those developed for stony asteroids (30; 49). Objects with  $D < 0.1 \text{ km}$  were placed into a “trash bin”; most were assumed to have been ground down to sizes small enough to be removed by radiation pressure or Poynting-Robertson drag (14, 20).

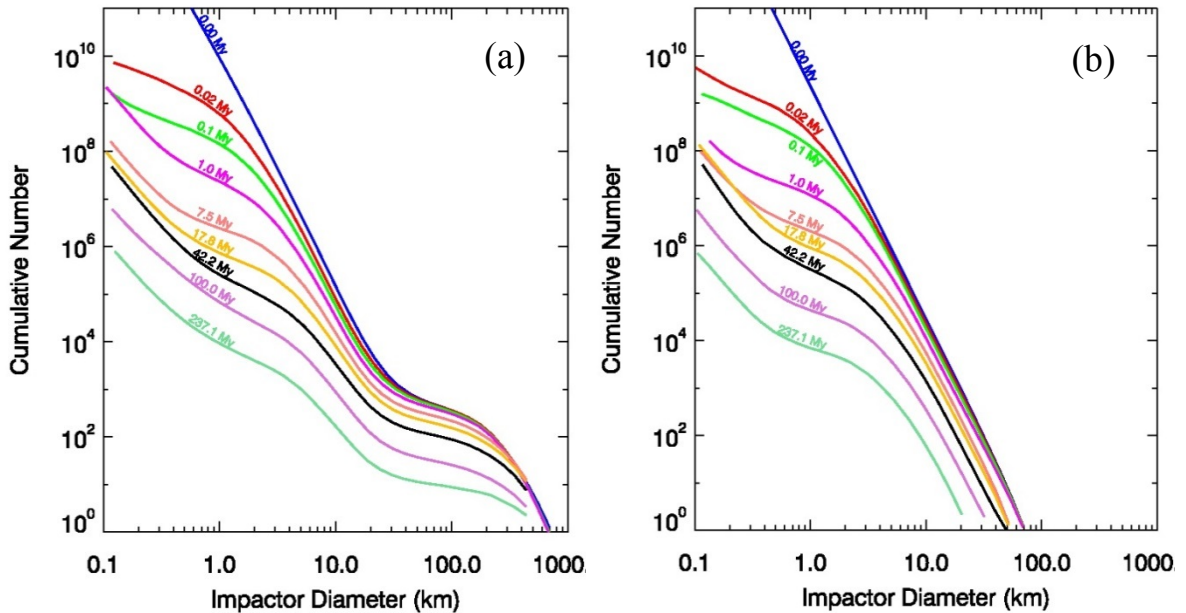


**Figure S8.** The collision and dynamical evolution of giant impact ejecta in the *Boulder* code (19). While undergoing comminution, the populations dynamically lose material according to Fig. S4.

- a) The initial cumulative SFD of GI ejecta was given power law exponents of -4.3, -4.9, -5.5, -0.8, and -3.5 at inflection points of  $D = 1.25, 10, 20, 170,$  and  $600 \text{ km}$ , respectively. The net mass of  $D > 0.1 \text{ km}$  bodies was set to 0.5% of an Earth mass. The inflection point at  $D = 1.25 \text{ km}$  helps keep the mass in the SFD fairly limited, while the point at  $D = 10 \text{ km}$  can be used to modify precisely how many km-sized impactors return to strike the Moon. The inflection points near  $D = 20 \text{ km}$  and  $170 \text{ km}$  were set so the lunar impacting population could plausibly make  $\sim 25$  Pre-Necarian lunar basins as well as South-Pole Aitken basin. The evolution time is labeled for each curve.
- b) A simpler initial cumulative SFD with a power law exponent of -4.9. The net mass of  $D > 0.1 \text{ km}$  bodies was set to  $\sim 3\%$  of an Earth mass, higher than before because we removed the inflection point at  $D = 1.25 \text{ km}$ . This population would make fewer large lunar basins. We find both SFDs evolve in similar ways. The differences seen are mainly a byproduct of stochastic disruption events.

Two representative examples of our model results are shown in Fig. S8. Using initial SFDs similar to those discussed above, we find that the  $D < 1$  km population is quickly decimated, losing two orders of magnitude in mass within 0.01-0.1 Myr of the GI. From there, the GI ejecta SFDs enter into a quasi-steady state shape that decays from collisional and dynamical evolution. Our  $D > 20$  km bodies are found to undergo little collisional evolution, as seen by the similarity between their loss rate and those for  $D > 170$  km bodies. These bodies appear to have little effect on the evolution of the  $D < 20$  km ejecta fragments.

**Inferences from these results.** Our work above suggests the following:

- Early collisional evolution of GI ejecta is extremely intense. Our test results, including many not shown, suggest nearly any steep slopes chosen for  $D < 20$  km would produce broadly similar results. Thus, our model results are only modestly dependent on the slope of the  $D < 20$  km SFD.
- If an inflection point at smaller sizes like the one shown in Fig. S8a is reasonable, and we believe this likely, the amount of solid debris in GI ejecta could be considerably less than 1% of an Earth mass. This would potentially allow high energy GI events (4-5), with much of their ejecta mass in the form of vapor, to produce numerous  $D > 10$  km craters on main belt asteroids.
- The precise nature of the  $D < 1$  km ejecta SFD may be of lesser importance for this problem because collisional evolution eliminates most of these bodies over very short time scales. This suggests the shock heating profiles shown in Fig. S5 are reasonably robust.

### Sec. 3. Impact Ages for Chondritic Meteorites and Lunar Samples

**Chondrite impact age data.** The  $^{40}\text{Ar}$ - $^{39}\text{Ar}$  shock degassing age probability distribution for 34 ordinary and enstatite chondrites, with mean ages between  $\sim 4.35$ - $4.56$  Ga, are shown in Fig. S9a (9-11). These data were used to construct the probability distributions shown in Fig. 2a, and they describe impact ages for at least six different undifferentiated parent bodies: EH, EL, enstatite melt clasts and aubrites, H, L, and LL. All of these parent bodies were presumably smaller than Vesta.

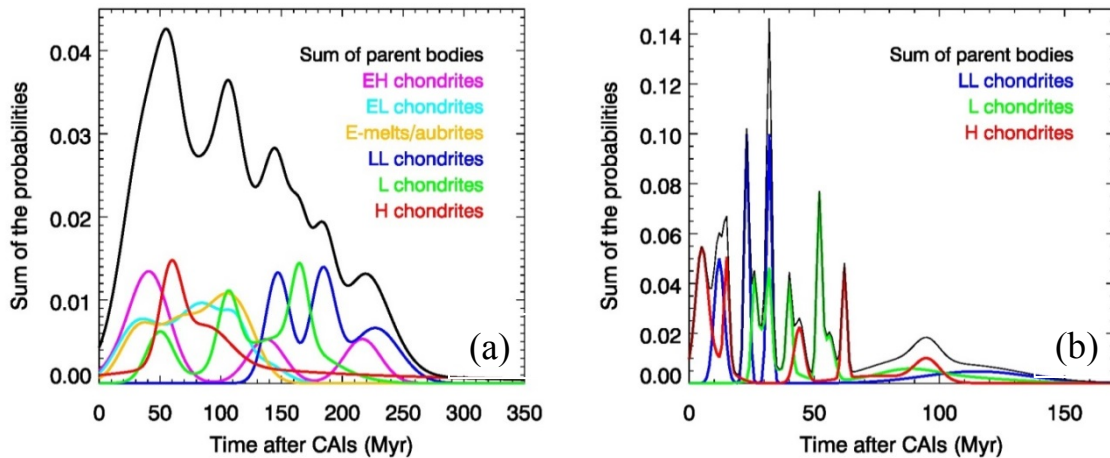


**Figure S9.** A more detailed look at the compilations of impact ages shown in Fig. 2.

- The  $^{40}\text{Ar}$ - $^{39}\text{Ar}$  shock degassing age-probability distribution for 34 ordinary and enstatite chondrites with mean ages between  $\sim 4.32$ - $4.567$  Ga. They represent sample ages for at least 5-6 parent bodies (EL, EH, E-melt/Aubrites, LL, L, and H chondrites). For each meteorite class, we computed the sum probability of ages as discussed in Fig. 2. The normalized profiles are shown by the colored curves, with their sum the black curve.
- The U-Pb age-probability distributions for 24 ordinary chondrites representing three parent bodies (LL, L, H chondrites). The ages  $> 60$  Myr after CAIs are thought to be from impact, while the ages  $< 60$  Myr after CAI ages are a mix of crystallization, metamorphic, and impact ages.

Few  $^{40}\text{Ar}$ - $^{39}\text{Ar}$  shock degassing ages are found between  $\sim 4.1$ - $4.4$  Ga, though there are many between  $3.5$ - $4.1$  Ga (9-12) (e.g., Fig. S10). The younger age set is thought to be associated with the so-called late heavy bombardment of our Solar System, as discussed and modeled in (12).

The U-Pb age probability distribution for 24 chondritic samples are shown in Figs. 2b and S9b. The ages of the samples are provided in Table S1. Many of the ages between 0-60 Myr after CAIs most likely came from simple parent body cooling (i.e., the parent bodies heat up after their formation, possibly by the decay of the radioactive isotope  $^{26}\text{Al}$ , but they eventually cool below the phosphate (apatite) closure temperature of 800 K). In terms of U-Pb ages, chondrite parent body cooling is thought to be complete for most near-surface materials by 60 Myr after CAIs (e.g., 32). This implies that younger U-Pb ages are solely derived from impact.

**Table S1.** U-Pb ages for ordinary chondrites as shown in Figs. 2b and S9b.

Number	Meteorite	Type	Age (Ma)	Reference	Reference #
1	Ste. Marguerite	H4	4563	(Göpel et al., 1994)	(50)
2	Nadiabondi	H5	4556-4566	(Göpel et al., 1994)	(50)
3	Forest Vale	H4	4561	(Göpel et al., 1994)	(50)
4	Allegan	H5	4550-4556	(Göpel et al., 1994)	(50)
5	St. Séverin	LL6	4554-4557	(Göpel et al., 1994)	(50)
6	Richardton	H5	4551-4553	(Göpel et al., 1994)	(50)
7	Tuxtuac	LL5	4544-4545	(Göpel et al., 1994)	(50)
8	Knyahinya	L5	4540-4543	(Göpel et al., 1994)	(50)
9	Barwell	L6	4538	(Göpel et al., 1994)	(50)
10	Elenovka	L5	4535 ± 1	(Amelin 2000)	(51)
11	Guider	LL5	4535-4536	(Göpel et al., 1994)	(50)
12	Saratov	L4	4530 ± 7	(Sprung et al. 2011)	(52)
13	Ausson	L5	4527-4528	(Göpel et al., 1994)	(50)
14	Kernouvé	H6	4521-4524	(Göpel et al., 1994)	(50)
15	Brudderheim	L6	4515 ± 1	(Sprung et al. 2010)	(53)
16	Homestead	L5	4514-4515	(Göpel et al., 1994)	(50)
17	Marion (Iowa)	L6	4511	(Göpel et al., 1994)	(50)
18	Guareña	H6	4504-4506	(Göpel et al., 1994)	(50)
19	Estacado	H6	4492 ± 15	(Blinova et al. 2007)	(54)
20	Mezo-Madaras	L3	4480±11	(Hanan and Tilton, 1985)	(55)
21	Sharps	H3	4472±5	(Hanan and Tilton, 1985)	(55)
22	Novato	L6	4472±31	(Yin et al., 2014)	(56)
23	Sahara 98222	L6	4467±22	(Ozawa et al., 2009)	(57)
24	Chelyabinsk	LL5	4452±21	(Popova et al., 2013)	(58)
Not Plotted	Chelyabinsk	LL5	4456±18	(Lapen et al., 2014)	(59)

We combined the chondrite data in our age-probability distributions because impact cratering is stochastic. We would expect that an age distribution from multiple parent bodies would be more likely to be representative of the dynamics of the main belt as a whole than would be the ages from a single asteroid.

**Eucrite and howardite ages.** The  $^{40}\text{Ar}$ - $^{39}\text{Ar}$  ages of eucrites and howardites are shown in Fig. S10, with the details and references discussed in (12). Each dated sample is reported with a gaussian profile with center and width corresponding to the most probable age and 1- $\sigma$  error. Profiles are color coded according to the class of the parent meteorites (retrieved from the on-line Meteoritical Bulletin database, Oct. 2011): unbrecciated eucrite (E-unbr), cumulate eucrite (E-cm), polymict (E-pmict) and monomict eucrites (E-

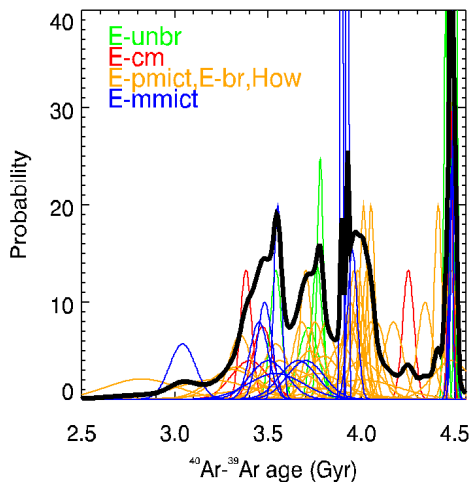


**Figure S10.** The  $^{40}\text{Ar}$ - $^{39}\text{Ar}$  ages of eucrites and howardites as compiled by (12).

mmict), brecciated eucrite (E-br) and howardites (How). The black curve is the sum probability distribution obtained by the sum of all gaussians divided by 5.

Most eucrites that show few signs of impact alteration (unbrecciated, cumulate, monomict) have ages of  $\sim 4.48$  Gyr ago. They are arguably consistent with being derived as quench ages as discussed in the main text. We argue this age spike is related to the features seen and  $\sim 95$  and  $106$  Myr after CAIs from Figs. 2 and S9.

**Discussion of chondrite impact ages.** For the data in Figs. 2 and S9, we have tried to separate out metamorphic ages from impact ages where possible. For the U-Pb data, this was done by pointing out that the data with ages  $> 60$  Myr after CAIs have been interpreted by experts as being solely produced by impact (32). For the  $^{40}\text{Ar}$ - $^{39}\text{Ar}$  reset ages in chondrites, there are several meteorites with clear indications of shock that have ages in the older range, so those ages are likely to be from impact as well. We cannot rule out the possibility that there are chondrites that lack strong indicators of shock whose ages are nonetheless impact ages because a collision removed material overlying them and initiated rapid cooling, as we have suggested for the eucrite meteorites. The lower closer temperature of the K-Ar system, however, means that  $^{40}\text{Ar}$ - $^{39}\text{Ar}$  metamorphic ages extend to significantly later times than U-Pb ages, so there is more overlap in time between metamorphism and the potential GI bombardment. For example,  $^{40}\text{Ar}$ - $^{39}\text{Ar}$  ages of feldspar from unshocked H6 chondrites, presumed to be metamorphic ages, cluster at  $\sim 4450$  Ma, while the Pb-Pb ages of phosphates from the same meteorites are  $\sim 4500$ - $4520$  Ma (60).

**Decay constants for  $^{40}\text{Ar}$ - $^{39}\text{Ar}$  data.** All  $^{40}\text{Ar}$ - $^{39}\text{Ar}$  data comes from laboratories using the value for the  $^{40}\text{K}$  decay constant defined by (61). Comparisons over the years with other geochronometers suggest that this value may not be correct (60, 62-65). Using values favored by some recent authors would lead to a systematic shift of all ages to values that are 10-30 Myr closer to the formation of the Solar System (i.e., 30 Myr for (60); 10-20 Myr for (62), and 15-20 Myr for (63-65)). This would shift the timing of the GI to younger values, but it would not affect the structure of the distribution of ages that suggest an event took place.

Interestingly, the peak in the  $^{40}\text{Ar}$ - $^{39}\text{Ar}$  age probability distribution in Figs. 2a and S9a is at 106 Myr after CAIs, while the equivalent peak for U-Pb in Figs. 2b and S9b is at  $\sim 95$

Myr after CAIs. This shift to younger ages by ~11 Myr may suggest that using a different  $^{40}\text{K}$  decay constant could lead to better agreement between the  $^{40}\text{Ar}$ - $^{39}\text{Ar}$  and U-Pb data sets. Nevertheless, we have not made any correction in our results, partly because there is not yet a consensus about the value of the  $^{40}\text{K}$  decay constant but also because the shift to younger ages would not change our basic results.

### Comparisons between predictions for the giant impact and ancient lunar samples.

Here we show several predicted times for the GI against the ages of the oldest lunar samples compiled by (66) (Fig. S11).

- The black line is our predicted GI age, which comes from (i) our analysis of  $^{40}\text{Ar}$ - $^{39}\text{Ar}$  shock degassing data (Figs. 2a, 3b, S9a), (ii) data from the chondritic U-Pb ages (Fig. 2b, S9b) and (iii) the  $^{40}\text{Ar}$ - $^{39}\text{Ar}$  ages of the eucrites and howardites (Fig. S10).
- Our model predictions for the chondrite  $^{40}\text{Ar}$ - $^{39}\text{Ar}$  shock degassing ages from the main text are shown in red at the top of Fig. S11.
- The remaining GI ages are derived from a wide variety of methods and samples (67-70). We caution that this list is not comprehensive; the interested reader can find many more predictions in the literature.

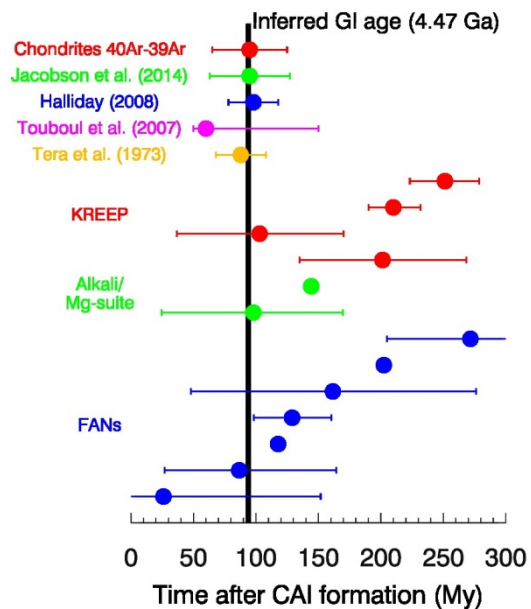


**Figure S11.** Comparison between derived ages for lunar samples, Moon-formation ages derived from sample data, and our best-fit Moon-formation age.

Here we assume the plotted lunar sample ages are a reasonably accurate representation of their formation age, which some contest (66). None are found to exceed the predicted GI age within errors. The plotted samples with the smallest error bars are also younger than our predicted GI age.

Overall, this correspondence suggests it is reasonable to assume there was a minimal time interval between the formation of the Moon and the most ancient lunar samples.

## References and Notes

1. W. F. Bottke, R. J. Walker, J. M. D. Day, D. Nesvorný, L. Elkins-Tanton, Stochastic late accretion to Earth, the Moon, and Mars. *Science* **330**, 1527–1530 (2010). [Medline doi:10.1126/science.1196874](#)
2. S. Marchi, W. F. Bottke, L. T. Elkins-Tanton, M. Bierhaus, K. Wünnemann, A. Morbidelli, D. A. Kring, Widespread mixing and burial of Earth's Hadean crust by asteroid impacts. *Nature* **511**, 578–582 (2014). [Medline doi:10.1038/nature13539](#)
3. R. M. Canup, Lunar-forming collisions with pre-impact rotation. *Icarus* **196**, 518–538 (2008). [doi:10.1016/j.icarus.2008.03.011](#)
4. M. Čuk, S. T. Stewart, Making the Moon from a fast-spinning Earth: A giant impact followed by resonant despinning. *Science* **338**, 1047–1052 (2012). [Medline doi:10.1126/science.1225542](#)
5. R. M. Canup, Forming a Moon with an Earth-like composition via a giant impact. *Science* **338**, 1052–1055 (2012). [Medline doi:10.1126/science.1226073](#)
6. D. D. Durda, W. F. Bottke Jr., D. Nesvorný, B. L. Enke, W. J. Merline, E. Asphaug, D. C. Richardson, Size-frequency distributions of fragments from SPH/ N-body simulations of asteroid impacts: Comparison with observed asteroid families. *Icarus* **186**, 498–516 (2007). [doi:10.1016/j.icarus.2006.09.013](#)
7. D. Nesvorný, Nesvorný HCM Asteroid Families V2.0 NASA Planetary Data System, (2012).
8. Materials and methods are available as supplementary materials on *Science* Online.
9. D. D. Bogard, K-Ar ages of meteorites: Clues to parent-body thermal histories. *Chem. Erde Geochem.* **71**, 207–226 (2011). [doi:10.1016/j.chemer.2011.03.001](#)
10. T. D. Swindle, D. A. Kring, J. R. Wierich, “ $^{40}\text{Ar}$ - $^{39}\text{Ar}$  ages of impacts involving ordinary chondrite meteorites,” in *Advances in  $^{40}\text{Ar}/^{39}\text{Ar}$  Dating: from Archeology to Planetary Sciences*, Geological Society of London, Special Publications, **378**, 333–347. (2013)
11. J. Hopp, M. Trierloff, U. Ott, E. V. Korochantseva, A. I. Buykin,  $^{39}\text{Ar}$ - $^{40}\text{Ar}$  chronology of the enstatite chondrite parent bodies. *Meteorit. Planet. Sci.* **49**, 358–372 (2014). [doi:10.1111/maps.12243](#)
12. S. Marchi, W. F. Bottke, B. A. Cohen, K. Wünnemann, D. A. Kring, H. Y. McSween, M. C. De Sanctis, D. P. O'Brien, P. Schenk, C. A. Raymond, C. T. Russell, High-velocity collisions from the lunar cataclysm recorded in asteroidal meteorites. *Nat. Geosci.* **6**, 303–307 (2013). [doi:10.1038/ngeo1769](#)
13. W. F. Bottke, H. F. Levison, D. Nesvorný, L. Dones, Can planetesimals left over from terrestrial planet formation produce the lunar Late Heavy Bombardment? *Icarus* **190**, 203–223 (2007). [doi:10.1016/j.icarus.2007.02.010](#)
14. A. P. Jackson, M. C. Wyatt, Debris from terrestrial planet formation: The Moon-forming collision. *Mon. Not. R. Astron. Soc.* **425**, 657–679 (2012). [doi:10.1111/j.1365-2966.2012.21546.x](#)

15. J. N. Connelly, M. Bizzarro, A. N. Krot, Å. Nordlund, D. Wielandt, M. A. Ivanova, The absolute chronology and thermal processing of solids in the solar protoplanetary disk. *Science* **338**, 651–655 (2012). [Medline doi:10.1126/science.1226919](#)
16. D. E. Wilhelms, The geologic history of the Moon. *U.S. Geol. Surv. Prof. Pap.*, paper 1348 (1987).
17. W. F. Bottke, D. Vokrouhlický, D. Minton, D. Nesvorný, A. Morbidelli, R. Brasser, B. Simonson, H. F. Levison, An Archaean heavy bombardment from a destabilized extension of the asteroid belt. *Nature* **485**, 78–81 (2012). [Medline doi:10.1038/nature10967](#)
18. P. Schenk, D. P. O’Brien, S. Marchi, R. Gaskell, F. Preusker, T. Roatsch, R. Jaumann, D. Buczkowski, T. McCord, H. Y. McSween, D. Williams, A. Yingst, C. Raymond, C. Russell, The geologically recent giant impact basins at Vesta’s south pole. *Science* **336**, 694–697 (2012). [Medline doi:10.1126/science.1223272](#)
19. A. Morbidelli, W. F. Bottke, D. Nesvorný, H. F. Levison, Asteroids were born big. *Icarus* **204**, 558–573 (2009). [doi:10.1016/j.icarus.2009.07.011](#)
20. J. A. Burns, P. L. Lamy, S. Soter, Radiation forces on small particles in the solar system. *Icarus* **40**, 1–48 (1979). [doi:10.1016/0019-1035\(79\)90050-2](#)
21. H. Y. McSween Jr., R. P. Binzel, M. C. De Sanctis, E. Ammannito, T. H. Prettyman, A. W. Beck, V. Reddy, L. Le Corre, M. J. Gaffey, T. B. McCord, C. A. Raymond, C. T. Russell, Dawn; the Vesta-HED connection; and the geologic context for eucrites, diogenites, and howardites. *Meteorit. Planet. Sci.* **48**, 2090–2104 (2013). [doi:10.1111/maps.12108](#)
22. A. Morbidelli, B. Gladman, Orbital and temporal distributions of meteorites originating in the asteroid belt. *Meteorit. Planet. Sci.* **33**, 999–1016 (1998). [doi:10.1111/j.1945-5100.1998.tb01707.x](#)
23. W. F. Bottke, M. C. Nolan, R. Greenberg, R. A. Kolvoord, Velocity distribution among colliding asteroids. *Icarus* **107**, 255–268 (1994). [doi:10.1006/icar.1994.1021](#)
24. W. F. Bottke Jr., D. Vokrouhlický, D. P. Rubincam, D. Nesvorný, The Yarkovsky and YORP effects: Implications for asteroid dynamics. *Annu. Rev. Earth Planet. Sci.* **34**, 157–191 (2006). [doi:10.1146/annurev.earth.34.031405.125154](#)
25. T. Kennedy, F. Jourdan, A. W. R. Bevan, M. A. Mary Gee, A. Frew, Impact history of the HED parent body(ies) clarified by new  $^{40}\text{Ar}/^{39}\text{Ar}$  analyses of four HED meteorites and one anomalous basaltic achondrite. *Geochim. Cosmochim. Acta* **115**, 162–182 (2013). [doi:10.1016/j.gca.2013.03.040](#)
26. R. H. Jones, F. M. McCubbin, L. Dreeland, Y. Guan, P. V. Burger, C. K. Shearer, C. K. Shearer, Phosphate minerals in LL chondrites: A record of the action of fluids during metamorphism on ordinary chondrite parent bodies. *Geochim. Cosmochim. Acta* **132**, 120–140 (2014). [doi:10.1016/j.gca.2014.01.027](#)
27. M. M. Marinova, O. Aharonson, E. Asphaug, Mega-impact formation of the Mars hemispheric dichotomy. *Nature* **453**, 1216–1219 (2008). [Medline doi:10.1038/nature07070](#)

28. F. Nimmo, S. D. Hart, D. G. Korycansky, C. B. Agnor, Implications of an impact origin for the martian hemispheric dichotomy. *Nature* **453**, 1220–1223 (2008). [Medline](#)  
[doi:10.1038/nature07025](https://doi.org/10.1038/nature07025)
29. H. F. Levison, M. J. Duncan, The long-term dynamical behavior of short-period comets. *Icarus* **108**, 18–36 (1994). [doi:10.1006/icar.1994.1039](https://doi.org/10.1006/icar.1994.1039)
30. W. F. Bottke Jr., D. D. Durda, D. Nesvorný, R. Jedicke, A. Morbidelli, D. Vokrouhlický, H. F. Levison, Linking the collisional history of the main asteroid belt to its dynamical excitation and depletion. *Icarus* **179**, 63–94 (2005). [doi:10.1016/j.icarus.2005.05.017](https://doi.org/10.1016/j.icarus.2005.05.017)
31. W. F. Bottke, D. Nesvorný, R. E. Grimm, A. Morbidelli, D. P. O’Brien, Iron meteorites as remnants of planetesimals formed in the terrestrial planet region. *Nature* **439**, 821–824 (2006). [Medline](#) [doi:10.1038/nature04536](https://doi.org/10.1038/nature04536)
32. R. Canup, Planetary science: Lunar conspiracies. *Nature* **504**, 27–29 (2013). [Medline](#)  
[doi:10.1038/504027a](https://doi.org/10.1038/504027a)
33. R. M. Canup, Lunar-forming impacts: Processes and alternatives. *Philos. Trans. A Math. Phys. Eng. Sci.* **372**, 20130175 (2014). [Medline](#) [doi:10.1098/rsta.2013.0175](https://doi.org/10.1098/rsta.2013.0175)
34. N. Dauphas, C. Burkhardt, P. H. Warren, T. Fang-Zhen, Geochemical arguments for an Earth-like Moon-forming impactor. *Philos. Trans. A Math. Phys. Eng. Sci.* **372**, 20130244 (2014). [Medline](#) [doi:10.1098/rsta.2013.0244](https://doi.org/10.1098/rsta.2013.0244)
35. W. R. Ward, R. M. Canup, The evection resonance and the angular momentum of the Earth-Moon system. *Lunar Planet. Sci. Conf.* **44**, 3029 (2013).
36. J. Salmon, R. M. Canup, Accretion of the Moon from non-canonical discs. *Philos. Trans. A Math. Phys. Eng. Sci.* **372**, 20130256 (2014). [Medline](#) [doi:10.1098/rsta.2013.0256](https://doi.org/10.1098/rsta.2013.0256)
37. M. Touboul, I. S. Puchtel, R. J. Walker, 182W evidence for long-term preservation of early mantle differentiation products. *Science* **335**, 1065–1069 (2012). [Medline](#)  
[doi:10.1126/science.1216351](https://doi.org/10.1126/science.1216351)
38. S. Mukhopadhyay, Early differentiation and volatile accretion recorded in deep-mantle neon and xenon. *Nature* **486**, 101–104 (2012). [Medline](#) [doi:10.1038/nature11141](https://doi.org/10.1038/nature11141)
39. L. W. Bandermaann, S. F. Singer, Calculation of meteoroid impacts on Moon and Earth. *Icarus* **19**, 108–113 (1973). [doi:10.1016/0019-1035\(73\)90142-5](https://doi.org/10.1016/0019-1035(73)90142-5)
40. J. Meyer, L. Elkins-Tanton, J. Wisdom, Coupled thermal-orbital evolution of the early Moon. *Icarus* **208**, 1–10 (2010). [doi:10.1016/j.icarus.2010.01.029](https://doi.org/10.1016/j.icarus.2010.01.029)
41. F. Nimmo, E. M. A. Chen, Tidal dissipation in the early lunar magma ocean and its role in the evolution of the Earth-Moon system. *Lunar Planet. Sci. Conf.* **45**, 1459 (2014).
42. R. M. Canup, Dynamics of lunar formation. *Annu. Rev. Astron. Astrophys.* **42**, 441–475 (2004). [doi:10.1146/annurev.astro.41.082201.113457](https://doi.org/10.1146/annurev.astro.41.082201.113457)
43. R. W. K. Potter, G. S. Collins, W. S. Kiefer, P. J. McGovern, D. A. Kring, Constraining the size of the South Pole-Aitken basin impact. *Icarus* **220**, 730–743 (2012).  
[doi:10.1016/j.icarus.2012.05.032](https://doi.org/10.1016/j.icarus.2012.05.032)
44. G. A. Neumann *et al.*, The inventory of lunar impact basins from LOLA and GRAIL. *Lunar Planet. Sci. Conf.* **44**, 2379 (2013).

45. K. Miljković, M. A. Wieczorek, G. S. Collins, M. Laneuville, G. A. Neumann, H. J. Melosh, S. C. Solomon, R. J. Phillips, D. E. Smith, M. T. Zuber, Asymmetric distribution of lunar impact basins caused by variations in target properties. *Science* **342**, 724–726 (2013). [Medline doi:10.1126/science.1243224](https://doi.org/10.1126/science.1243224)
46. H. J. Melosh, *Impact Cratering*, Oxford Monographs on Geology and Geophysics no. 11 (Oxford Univ. Press, New York, 1989).
47. D. D. Durda, W. F. Bottke Jr., B. L. Enke, W. J. Merline, E. Asphaug, D. C. Richardson, Z. M. Leinhardt, The formation of asteroid satellites in large impacts: Results from numerical simulations. *Icarus* **170**, 243–257 (2004). [doi:10.1016/j.icarus.2004.04.003](https://doi.org/10.1016/j.icarus.2004.04.003)
48. E. Asphaug, Similar-sized collisions and the diversity of planets. *Chem. Erde Geochem.* **70**, 199–219 (2010). [doi:10.1016/j.chemer.2010.01.004](https://doi.org/10.1016/j.chemer.2010.01.004)
49. W. Benz, E. Asphaug, Catastrophic disruptions revisited. *Icarus* **142**, 5–20 (1999). [doi:10.1006/icar.1999.6204](https://doi.org/10.1006/icar.1999.6204)
50. C. Göpel, G. Manhes, C. J. Allegre, U-Pb systematics of phosphates from equilibrated ordinary chondrites. *Earth Planet. Sci. Lett.* **121**, 153–171 (1994). [doi:10.1016/0012-821X\(94\)90038-8](https://doi.org/10.1016/0012-821X(94)90038-8)
51. Y. Amelin, U-Th-Pb systematics of chondritic phosphates: Implications for chronology and origin of excess Pb. *Lunar Planet. Sci. Conf.* **31**, 1201 (2000).
52. P. Sprung, C. Gopel, T. Kleine, J. A. van Orman, C. Maden, The high-temperature history and primary structure of the L chondrite parent body. *Lunar Planet. Sci. Conf.* **42**, 1850 (2011).
53. P. Sprung, C. Gopel, T. Kleine, J. A. van Orman, B. Bourdon, A Hf-W perspective on the thermal evolution of the L chondrite parent body. *Lunar Planet. Sci. Conf.* **41**, 1921 (2010).
54. A. Blinova, Y. Amelin, C. Samson, Constraints on the cooling history of the H-chondrite parent body from phosphate and chondrule Pb-isotopic dates from Estacado. *Meteorit. Planet. Sci.* **42**, 1337–1350 (2007). [doi:10.1111/j.1945-5100.2007.tb00578.x](https://doi.org/10.1111/j.1945-5100.2007.tb00578.x)
55. B. B. Hanan, G. R. Tilton, Early planetary metamorphism in chondritic meteorites. *Earth Planet. Sci. Lett.* **74**, 209–219 (1985). [doi:10.1016/0012-821X\(85\)90022-6](https://doi.org/10.1016/0012-821X(85)90022-6)
56. Q.-Z. Yin, Q. Zhou, Q.-L. Li, X.-H. Li, Y. Liu, G.-Q. Tang, A. N. Krot, P. Jenniskens, Records of the Moon-forming impact and the 470 Ma disruption of the L chondrite parent body in the asteroid belt from U-Pb apatite ages of Novato (L6). *Meteorit. Planet. Sci.* **49**, 1426–1439 (2014). [doi:10.1111/maps.12340](https://doi.org/10.1111/maps.12340)
57. S. Ozawa, E. Ohtani, K. Terada, Pressure and timing of the shock events recorded in L6 chondrites (2009) *Lunar Planet. Sci. Conf.* **40**, 1474 (2009).
58. O. P. Popova, P. Jenniskens, V. Emel'yanenko, A. Kartashova, E. Biryukov, S. Khaibrakhmanov, V. Shuvalov, Y. Rybnov, A. Dudorov, V. I. Grokhovsky, D. D. Badyukov, Q. Z. Yin, P. S. Gural, J. Albers, M. Granvik, L. G. Evers, J. Kuiper, V. Kharlamov, A. Solovyov, Y. S. Rusakov, S. Korotkiy, I. Serdyuk, A. V. Korochantsev, M. Y. Larionov, D. Glazachev, A. E. Mayer, G. Gisler, S. V. Gladkovsky, J. Wimpenny, M. E. Sanborn, A. Yamakawa, K. L. Verosub, D. J. Rowland, S. Roeske, N. W. Botto, J.

- M. Friedrich, M. E. Zolensky, L. Le, D. Ross, K. Ziegler, T. Nakamura, I. Ahn, J. I. Lee, Q. Zhou, X. H. Li, Q. L. Li, Y. Liu, G. Q. Tang, T. Hiroi, D. Sears, I. A. Weinstein, A. S. Vokhmintsev, A. V. Ishchenko, P. Schmitt-Kopplin, N. Hertkorn, K. Nagao, M. K. Haba, M. Komatsu, T. Mikouchi, Chelyabinsk Airburst Consortium, Chelyabinsk airburst, damage assessment, meteorite recovery, and characterization. *Science* **342**, 1069–1073 (2013). [Medline doi:10.1126/science.1242642](https://doi.org/10.1126/science.1242642)
59. T. J. Lapen, D. A. Kring, M. E. Zolensky, R. Andreasen, M. Richter, T. D. Swindle, S. P. Beard, Uranium-lead isotope evidence in the Chelyabinsk LL5 chondrite meteorite for ancient and recent thermal events. *Lunar Planet. Sci. Conf.* **45**, 2561 (2014).
60. M. Tieloff, E. K. Jessberger, I. Herrwerth, J. Hopp, C. Fiéni, M. Ghélis, M. Bourot-Denise, P. Pellas, Structure and thermal history of the H-chondrite parent asteroid revealed by thermochronometry. *Nature* **422**, 502–506 (2003). [Medline doi:10.1038/nature01499](https://doi.org/10.1038/nature01499)
61. R. H. Steiger, E. Jäger, Subcommittee on geochronology: Convention on the use of decay constants in geo- and cosmochronology. *Earth Planet. Sci. Lett.* **36**, 359–362 (1977). [doi:10.1016/0012-821X\(77\)90060-7](https://doi.org/10.1016/0012-821X(77)90060-7)
62. N. Vogel, P. R. Renne,  $^{40}\text{Ar}$ - $^{39}\text{Ar}$  dating of plagioclase grain size separates from silicate inclusions in IAB iron meteorites and implications for the thermochronological evolution of the IAB parent body. *Geochim. Cosmochim. Acta* **72**, 1231–1255 (2008). [doi:10.1016/j.gca.2007.12.001](https://doi.org/10.1016/j.gca.2007.12.001)
63. P. R. Renne, R. Mundil, G. Balco, K. Min, K. R. Ludwig, K. R. Ludwig Joint determination of 40K decay constants and  $^{40}\text{Ar}/^{40}\text{K}$  for the Fish Canyon sanidine standard, and improved accuracy for  $^{40}\text{Ar}/^{39}\text{Ar}$  geochronology. *Geochim. Cosmochim. Acta* **74**, 5349–5367 (2010). [doi:10.1016/j.gca.2010.06.017](https://doi.org/10.1016/j.gca.2010.06.017)
64. P. R. Renne, G. Balco, K. R. Ludwig, R. Mundil, K. Min, Response to the comment by W. H. Schwarz *et al.* on “Joint determination of 40K decay constants and  $^{40}\text{Ar}^*/^{40}\text{K}$  for the Fish Canyon sanidine standard, and improved accuracy for  $^{40}\text{Ar}/^{39}\text{Ar}$  geochronology” by P. R. Renne *et al.* (2010). *Geochim. Cosmochim. Acta* **75**, 5097–5100 (2011). [doi:10.1016/j.gca.2011.06.021](https://doi.org/10.1016/j.gca.2011.06.021)
65. W. H. Schwarz, K. Kossert, M. Tieloff, J. Hopp, Comment on the “Joint determination of 40K decay constants and  $^{40}\text{Ar}^*/^{40}\text{K}$  for the Fish Canyon sanidine standard, and improved accuracy for  $^{40}\text{Ar}/^{39}\text{Ar}$  geochronology” by Paul R. Renne *et al.* (2010). *Geochim. Cosmochim. Acta* **75**, 5094–5096 (2011). [doi:10.1016/j.gca.2011.06.022](https://doi.org/10.1016/j.gca.2011.06.022)
66. L. E. Borg, J. N. Connelly, M. Boyet, R. W. Carlson, Chronological evidence that the Moon is either young or did not have a global magma ocean. *Nature* **477**, 70–72 (2011). [Medline doi:10.1038/nature10328](https://doi.org/10.1038/nature10328)
67. F. Tera, D. A. Papanastassiou, G. J. Wasserburg, A lunar cataclysm at 3.95 AE and the structure of the lunar crust. *Lunar Planet. Sci. Conf.* **4**, 723 (1973).
68. M. Touboul, T. Kleine, B. Bourdon, H. Palme, R. Wieler, Late formation and prolonged differentiation of the Moon inferred from W isotopes in lunar metals. *Nature* **450**, 1206–1209 (2007). [Medline doi:10.1038/nature06428](https://doi.org/10.1038/nature06428)

69. A. N. Halliday, A young Moon-forming giant impact at 70-110 million years accompanied by late-stage mixing, core formation and degassing of the Earth. *Philos. Trans. A Math. Phys. Eng. Sci.* **366**, 4163–4181 (2008). [Medline doi:10.1098/rsta.2008.0209](https://doi.org/10.1098/rsta.2008.0209)
70. S. A. Jacobson, A. Morbidelli, S. N. Raymond, D. P. O'Brien, K. J. Walsh, D. C. Rubie, Highly siderophile elements in Earth's mantle as a clock for the Moon-forming impact. *Nature* **508**, 84–87 (2014). [Medline doi:10.1038/nature13172](https://doi.org/10.1038/nature13172)